NANO LETTERS

Letter

pubs.acs.org/NanoLett

Quantum Junction Solar Cells

Jiang Tang,[†,∥] Huan Liu,[‡,∥] David Zhitomirsky,[§] Sjoerd Hoogland,[§] Xihua Wang,[§] Melissa Furukawa,[§] Larissa Levina,[§] and Edward H. Sargent*[,§]

[†]Wuhan National Laboratory for Optoelectronics and [‡]School of Optical and Electronic Information, Huazhong University of Science and Technology, 1037 Luoyu Road, Wuhan, Hubei 430074, China

[§]Department of Electrical and Computer Engineering, University of Toronto, 10 King's College Road, Toronto, Ontario, M5S 3G4, Canada

Supporting Information

ABSTRACT: Colloidal quantum dot solids combine convenient solution-processing with quantum size effect tuning, offering avenues to high-efficiency multijunction cells based on a single materials synthesis and processing platform. The highest-performing colloidal quantum dot rectifying devices reported to date have relied on a junction between a quantum-tuned absorber and a bulk material (e.g., TiO_2); however, quantum tuning of the absorber then requires complete redesign of the bulk acceptor, compromising the benefits of facile quantum tuning. Here we report rectifying junctions constructed entirely using inherently band-aligned quantum-tuned materials. Realizing these quantum junction diodes relied upon the creation of an n-type quantum dot solid having a clean bandgap. We combine stable, chemically compatible, high-performance n-type and p-type materials to create the first quantum junction solar cells. We present a family of photovoltaic devices having widely tuned bandgaps of 0.6−1.6 eV that excel where conventional quantum-to-bulk devices fail to perform. Devices having optimal single-junction bandgaps exhibit certified AM1.5 solar power conversion efficiencies of 5.4%. Control over doping in quantum solids, and the successful integration of these materials to form stable quantum junctions, offers a powerful new degree of freedom to colloidal quantum dot optoelectronics.

KEYWORDS: *Colloidal quantum dots, PbS, homojunction, n-type, photovoltaics*

The broadband solar spectrum demands that solar cells be constructed using materials having an infrared bandgap. Benefiting from the single-junction Shockley-Queisser efficiency bound of 31% relies on a near-infrared bandgap in the range 1−1.5 eV.[1] Raising this limit using tandem and multijunction architectures requires a palette of bandgaps in the visible, near-infrared, and short-wavelength infrared.[2] To date, the bandgaps of light-absorbing semiconductors making up multijunction solar cells have been tuned primarily via control over composition, such as in GaInP/GaAs/GaInNAs triple-junction solar cell having record 43.5% efficiency under solar concentration.[3] This demands optimization of multiple materials sets within each junction. With facile tuning of the bandgap and ease of processing, colloidal quantum dots offer avenues to inexpensive and robust multijunction solar cell architectures.

Recently, quantum size-effect tuning was exploited to realize a tandem solar cell having optimal visible (1.6 eV) and infrared (1.0 eV) bandgaps.[4] These colloidal quantum dot (CQD) solar cells,[5−10] while attractive, suffer an important limitation: rigorous control over the bandedge of the electron-acceptor is critical to achieve high performance.[11] The band offset must be sufficient to support electron extraction, yet not so large as to compromise operating voltage. The resultant process window is a narrow ∼0.1 eV, demanding substantial reengineering to customize electrodes to the specifications necessitated by the newly quantum-tuned absorber.[11,12]

In summary, to date quantum tuning has benefited only the absorber. Because of the quantum-to-bulk mismatch, the benefit of quantum tuning has, at best, been half-realized.

Constructing a solar cell in which the junction itself is fully quantum-tuned would overcome this limitation. A quantum-junction solar cell (QJSC) would employ the same semiconductor, having the same degree of quantum tuning, on each side of the junction; the only change would be in doping character, from p- to n-type, leading to the establishment of a depletion region for efficient carrier separation and collection.

In the quantum junction, the p- and n-type layers are constructed from the same underlying material, ensuring band alignment for CQDs of any size (Figure 1a). In contrast, in the depleted-heterojunction device (Figure 1b), the p-type layer is composed of CQDs, and the n-type layer of an entirely different large-bandgap bulk transparent conductive oxide (TiO_2 as an example here). Using highly quantum-confined CQDs yields a large conduction band cliff relative to TiO_2, favoring electron extraction but at substantial cost to operating voltage. Using small-bandgap CQDs leads to an unfavorable junction spike that degrades current. We simulated (Figure 1c) the operating voltage, current, and performance of each architecture as a function of absorber layer bandgap via self-consistent optoelectronic modeling (Supporting Information S1). Current is lost in the conventional CQD device once the

Received: June 30, 2012
Revised: August 2, 2012
Published: August 10, 2012

   dx.doi.org/10.1021/nl302436r | *Nano Lett.* 2012, 12, 4889−4894

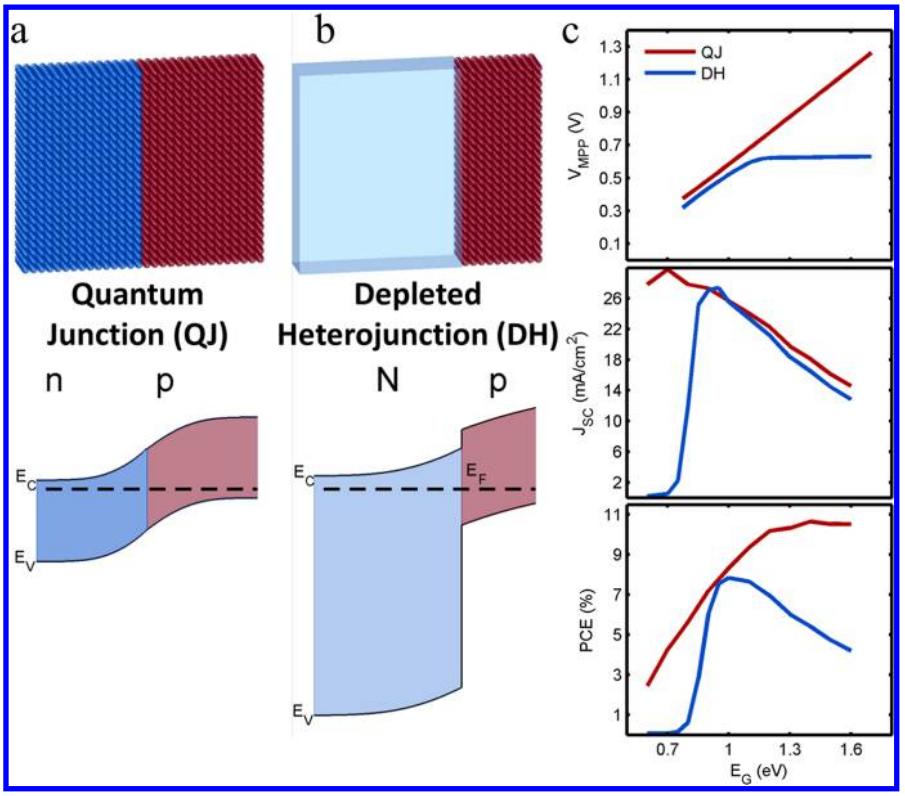

Figure 1. (a) In the quantum junction solar cell, size-effect tuning on each side of the junction achieves an inherent match in band alignments between n-type (blue) and p-type (red) materials. (b) In quantum-to-bulk devices such as the depleted-heterojunction solar cell, stoichiometric tuning of the n-type electron acceptor (blue) is required to achieve the precise band offset desired for optimal device operation. (c) Simulated (Supporting Information S1) solar cell performance, showing the operating voltage at the maximum power point, V_{MPP}, the short-circuit current, J_{SC}, and the solar power conversion efficiency, PCE, for each class of devices as a function of quantum dot bandgap.

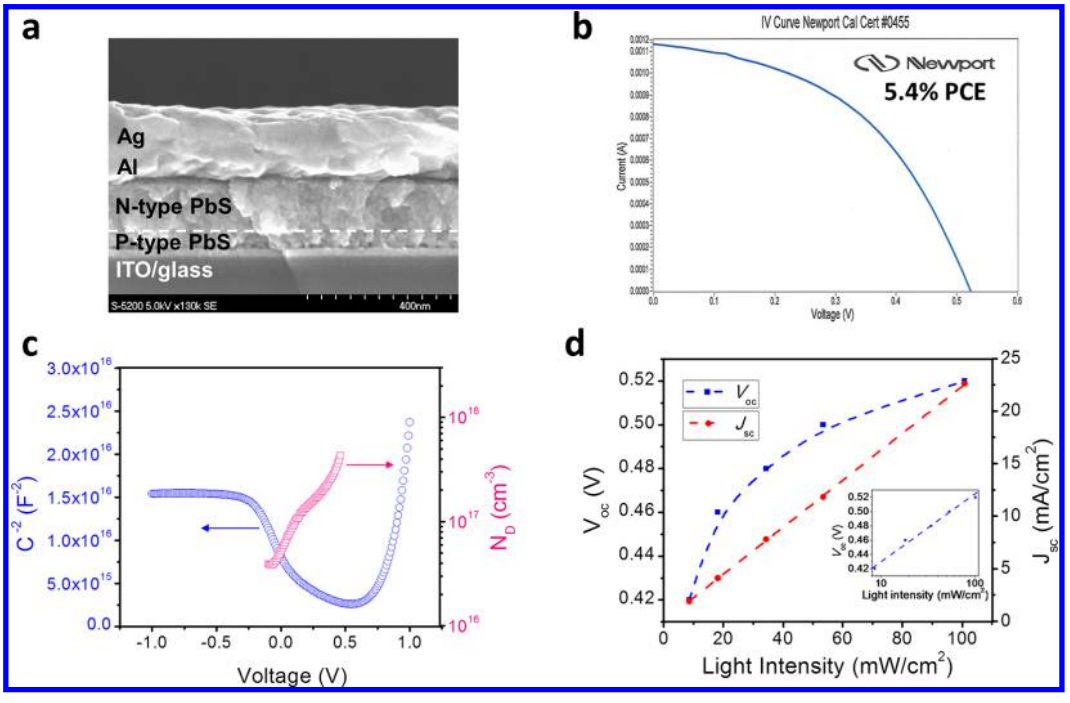

Figure 2. (a) Cross-sectional scanning electron micrograph of a completed device. The boundary between p-type and n-type PbS regions is highlighted using a white dashed line. (b) Device performance and *JV* curve measured 100 mW/cm^2 AM1.5 illumination. (c) The 1/capacitance^2 versus voltage and the corresponding derived n-type doping density range of the QJSC device. (d) V_{oc} and J_{sc} dependence on incident intensity. The inset is a semilogarithmic plot of V_{oc} versus light intensity.

band offset becomes unfavorable; and the operating voltage is optimal only at one single choice of bandgap. In contrast, the QJ device achieves optimal current, voltage, and power across a wide range of bandgaps important in solar harvesting. The

dx.doi.org/10.1021/nl302436r | *Nano Lett.* 2012, 12, 4889−4894

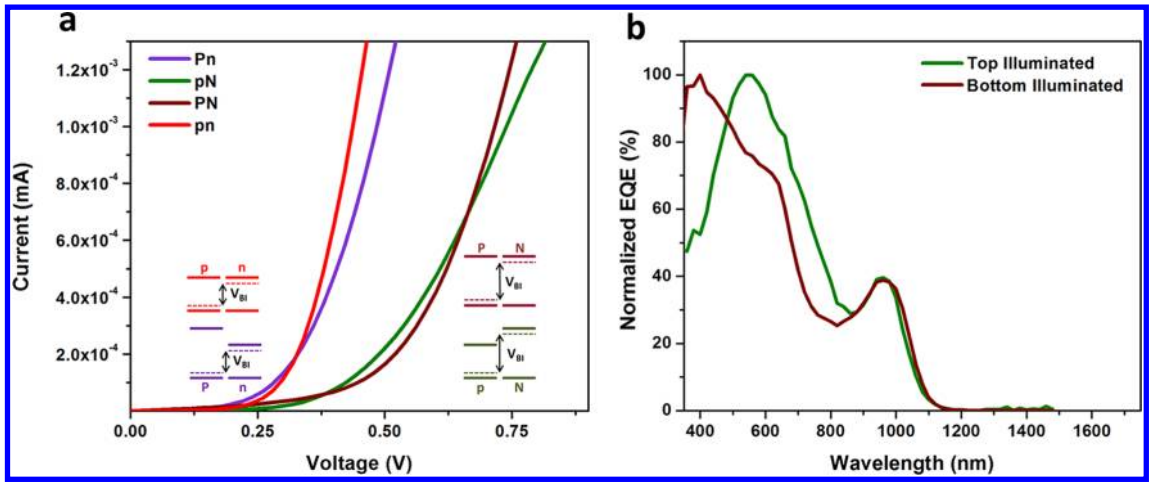

Figure 3. (a) Junctions constructed by varying the quantum dot size between large and small bandgap material on each side of the junction resulting in different turn-on voltages. Insets: diagrams depicting the band alignments on each side of the junction and difference in work functions that result in the observed turn on voltages. (b) EQE spectra of top and bottom illuminated device showing the existence of a junction near the p-side, and the loss of QE if illumination is done on the n-side.

inherent quantum-to-quantum match enables wide control over bandgap while enforcing optimal energetic band alignment in a single materials system.

The appealing prospect of the QJSC has yet to be realized for an important reason. It demands that both p- and n-type semiconductors, each one of high quality in a photovoltaic context, be engineered using single CQD material. This dexterity of doping must be achieved using processes that are chemically compatible among layers and that result in materials that are stable, high in mobility, and low in trap density and depth.[13] Hydrazine treatment has been reported to convert PbSe CQD films from p- to n-type,[14] and Cd^{2+} doping converts n-type InAs CQDs to p-type.[15] Unfortunately, there exist no reports of photovoltaic devices made using n-type colloidal quantum dot solids.

To build a QJ device, we form the n- side of our junction by employing a PbS layer treated with a halide in an inert environment to yield n-type films.[16] We also required a highly robust p-type CQD film, one that would not lose its strong p-type doping when layers on top of it were treated under n-doping conditions. We used tetramethylammonium hydroxide in ambient, combined with air annealing, to maximize oxygen binding and thus p-doping.[17] To investigate the possibility that p-doping would be reversed during the subsequent addition of the n-type film, we further demonstrated that the p-type character, and the full extent of the high doping, were fully retained following soaking in halide solution for 10 min (Supporting Information S2), as required to build a p-type bottom layer followed by n-type top layers to form a QJ device.

We now turn to the realization of the full QJ devices. A successful architecture would rely on ohmic contacts to each of the n-type and p-type colloidal quantum dot solids, and the formation of a stable and robust rectifying junction between our p- and n-type materials, without unacceptable diffusion and chemical reactivity among the layers. We began with a transparent conductive indium tin oxide (ITO) electrode on a glass substrate (Figure 2a). The ITO forms an ohmic contact to the heavily p-type CQD bottom layer. For the n-type layer,[16] we selected an iodide treatment whose low net doping would produce a thick depletion region and whose high carrier mobility would ensure efficient carrier extraction and maximize fill factor. A shallow-work-function metal aluminum top contact collected electrons from the n-type upper layer.

A typical high-performing device employed 50 nm thick p-type beneath 300 nm thick n-type colloidal quantum dot film. Absorbance spectra show that quantum confinement is retained (Supporting Information S6). The device exhibits a *JV* characteristic under AM1.5 simulated solar illumination (Figure 2b) that resulted in a certified power conversion efficiency (PCE), verified by an independent laboratory, of 5.4%. The certified performance includes a short circuit current density (JSC) of 22.2 mA/cm^2, open circuit voltage of 0.52 V, and a fill factor of 47%%; this result is the highest certified performance for PbS CQD solar cells compared to the 5.1%[18] record based on reports published at the time of submission of the present work.

The layer-by-layer approach of interfacing the two materials yielded robust and functional devices, attributable to the stable p-layer and the selection of a lightly doped n-layer formed using a mild chemical treatment. Mott−Schottky capacitance−voltage characterization[19] (Figure 2c and Supporting Information S3) indicated an n-type doping density on the order of 10^{16}−10^{17} cm^{-3}. Because the capacitance−voltage plot does not exhibit a defined linear region, we report a range for the estimated doping density based on the slope at each point along the curve. This allows us to provide an order-of-magnitude estimate of the doping of the lower-doped side of the junction, the n-side in our device.

The depletion region extends well into the n-layer, as attested to by the observation that as the device is nearly at full depletion at 0 V. The intensity-dependent performance (Figure 2d) showed a linear dependence of J_{sc} on light intensity, proving that the device operates below the bimolecular-recombination-limited and space-charge-accumulation-limited regimes.[20] V_{oc} increases logarithmically with light intensity, leading to increased device efficiency at elevated light intensity.

We devised a suite of experiments to investigate whether the devices did indeed operate based on the p-n junction principle proposed herein. When we removed either the p-type or the n-type quantum dot layer, devices lost rectification and had efficiency below 0.1% (Supporting Information S4). We also built quantum heterojunction diode, using either a large-

dx.doi.org/10.1021/nl302436r | *Nano Lett.* 2012, 12, 4889−4894

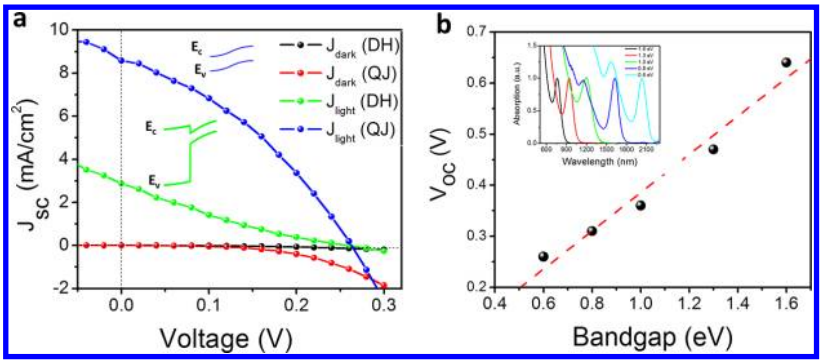

Figure 4. (a) Light and dark $J-V$ curves of quantum junction (QJ) and depleted heterojunction (DH) devices using 0.6 eV PbS CQDs. The DH device employed ZnO as the electron accepting layer and MPA treated PbS CQDs as the absorber layer. Inset diagrams show the favorable band alignment for QJ, and an adverse energy spike for the DH. (b) Dependence of measured QJSC device open-circuit voltage (black filled circles) on the bandgaps of PbS CQDs employed. The linear voltage dependence (red dashed line = fit) is consistent with the trends observed in Figure 1c. (Inset) Normalized absorption spectra of PbS CQDs employed in QJSCs. Bandgaps range from 0.6 to 1.6 eV, spanning the solar spectrum.

bandgap P- or N-layer combined with a small-bandgap n- or p-layer, and investigated the dark current−voltage characteristics, looking especially at the forward turn-on of the diode (Figure 3a). When the large-bandgap N-layer replaced the smaller-gap n-layer, a commensurable increase in turn-on voltage was observed. This agrees with the previously reported observation that quantum confinement primarily tunes the conduction band level upward in PbS and has much less impact on valence band energies.[21,22] Finally, we measured external quantum efficiency (EQE) for illumination from the p-side (bottom) and n-side (top) of the devices and present the normalized spectra for comparison (Figure 3b). For top illumination, the short-wavelength EQE was degraded. We concluded that these photons, mainly absorbed on the top of the thick n-layer, suffered from recombination before reaching the distant junction. For the bottom-illumination case, the external quantum efficiency is at a maximum at 400 nm wavelength. Since at least 40% of incident light at this wavelength is absorbed within the p-material, this confirms that the p-layer efficiently contributes to photocurrent.

In summary, only with both the p-type and n-type CQD films in place are rectification and a strong photovoltaic effect observed; changing the bandgap of one side of the quantum junction leads to a rationally predicted impact on turn-on voltage and the optoelectronic behavior of the devices is explainable with reference to our use of a thin p-layer and a thick n-layer. Photons absorbed on both the p- and the n-side of the device contribute appreciably to photocurrent; thus each is a good photovoltaic building-block material.

We sought to feature the versatility of the QJ concept by constructing families of devices with a wide range of all-quantum-tuned bandgaps. We explored the use of PbS CQDs having the following bandgaps: 1.6, 1.3, 1.0, 0.8, and 0.6 eV PbS. The absorption cutoff ranges from 770 to 2060 nm, spanning the solar spectrum (Figure 4b inset). The smallest-bandgap devices, those having a PbS CQD bandgap of 0.6 eV, exhibited an open-circuit voltage of 0.26 V (Figure 4a), achieving ~80% of the theoretical V_{oc} limit for a device having this bandgap (Supporting Information S5). Additionally, the open-circuit voltage of QJ devices showed a linear correlation with CQD bandgap (Figure 4b), consistent with theory.[1] Depleted-heterojunction solar cell made using the same size CQDs on a ZnO electrode exhibited half the current and half the fill factor of the QJSC. This is consistent with ZnO forming a heterojunction with the p-type CQDs that fails to favor electron extraction. It illustrates that the fixed-bandgap bulk electrode fails to offer versatile matching with the quantum-tuned solid. In contrast, the robust engineering of both p- and n-type materials in one materials system allowed quantum tuning and inherently matched band alignment, resulting in a range of highly efficient, custom-bandgap photovoltaic devices.

The QJSC device concept paves the way to tandem and triple-junction CQD solar cells made via monolithic stacking. The room-temperature solution-processing approach promises ready integration of QJSCs with other solar cell architectures such as amorphous silicon or polymer solar cells. Tunable band gap through the quantum-size effect, and independent tunability of the doping type through ligand engineering, enable a wide range of other electronic and optical devices, including bipolar junction transistors, thyristors, and graded-doping devices.

Methods. *Materials Preparation.* PbS CQDs of various sizes are fabricated following a published recipe.[23,24]

Film Deposition. Layer-by-layer spin-coating was applied to fabricate the CQD film. Deposition of the p-layer was carried out inside the fumehood: (1) 4 drops of PbS CQDs in octane (25 mg mL^{-1}) were dropped onto ITO glass substrates and were spin-cast at 2500 rpm for 10 s; (2) 0.75 mL of 10 mg/mL TMAOH methanol solution were deposited, followed by spin-coating 10 s at 2500 rpm; (3) 0.75 mL of methanol were dropped and spin-cast at 2500 rpm for 10 s (repeat twice). Steps 1−3 were repeated until the desired thickness of PbS CQDs films was reached. The as-deposited p-layer samples were annealed at 50 °C in air for 12 h and then transferred into an N_2-glovebox for n-layer deposition. Similar deposition protocols were employed to fabricate n-layers except that Tetrabutylammonium Ioidide in methanol was used in film treatment for 1 min.

Electrode Deposition. Al (30 nm thick) layer was deposited at a rate of 0.4 Å/s using thermal evaporation and sputtering, respectively, followed by thermal evaporation of silver contacts (200 nm thick) at a rate of 1.5 Å/s with base pressure of 1×10^{-7} mbar. The deposition was carried out in Angstrom Engineering Åmod deposition system in an Innovative Technology glovebox. Contact size of each pixel was 0.061 cm^2. Aluminum Zinc Oxide (AZO) was sputtered at 0.1A/s in an argon atmosphere. The base pressure was about 2e-7 Torr, while the Argon pressure was set to about 9 mTorr. The total AZO thickness was 100 nm.

dx.doi.org/10.1021/nl302436r | *Nano Lett.* 2012, 12, 4889−4894

Field Effect Transistor (FET) Measurement. Commercial silicon wafers (highly doped p-type using boron) with a thin layer of thermally oxidized SiO_2 were used as substrates and gate dielectric. Au and Al (or Ag) are used as the source and drain electrodes to form the ohmic contact to p-type and n-type materials, respectively, at a thickness of 100 nm. For bottom-contacted FET studies, prepatterned Au contacts were used with a channel length of 5 μm and channel width of 1 mm. Top-contacted FET devices employed thermal evaporation of Al or Ag through a shadow mask to create channel lengths of 25 and 50 μm and channel widths of 500 and 100 um. The deposition of CQDs was carried out using the same protocols as in QJSC devices.

PCE Characterization. Current−voltage characteristics were measured using a Keithley 2400 source-meter in N_2 ambient. The solar spectrum at AM1.5 was simulated to within class A specifications (less than 25% spectral mismatch) with a Xe lamp and filters (Solar Light Company Inc.) with measured intensity at 100.6 mW cm^{-2}. The source intensity was measured using a Melles-Griot broadband power meter and a Thorlabs broadband power meter through a circular 0.05 cm^2 aperture at the position of the device and confirmed with a calibrated reference solar cell (Newport, Inc.). The accuracy of the power measurement was estimated to be ±5%.

EQE Characterization. The incident spectrum for EQE measurements was generated by passing the output of a 400 W Xe (Horiba Jobin-Yvon) lamp through a monochromator (Horiba Jobin-Yvon FL-1039) and using appropriate order-sorting filters (Newport). The resultant monochromatic beam also passed through an optical chopper operating at 100 Hz coupled to the input of a Stanford Research Systems lock-in amplifier. The collimated output of the monochromator was measured through a 0.05 cm^2 aperture with calibrated Newport 818-UV and Newport 818-IR power meters as needed. The measurement step was 20 nm and the intensity varied with the spectrum of the Xe lamp. The photogenerated current was then measured using a lock-in amplifier. Top illumination and EQE of devices was done by employing a transparent low work function aluminum zinc oxide electrode atop the n-layer.

Cap-V Measurement. The capacitance−voltage measurements were performed directly on the photovoltaic devices using an Agilent 4284A LCR meter at a high frequency of 20 kHz. The scanning voltage was −1.0 to 1.0 V.

Absorbance Measurement. Absorbance measurements were carried out on films fabricated using a layer-by-layer procedure to a total thickness of ∼250 nm. Cary 500 UV−vis spectrometer was used to acquire the spectra.

■ ASSOCIATED CONTENT

Ⓢ Supporting Information

Supporting materials 1−6 are outlined in the document accompanying this manuscript. This material is available free of charge via the Internet at http://pubs.acs.org.

■ AUTHOR INFORMATION

Corresponding Author

*E-mail: ted.sargent@utoronto.ca.

Author Contributions

‖These authors contributed equally.

Notes

The authors declare no competing financial interest.

■ ACKNOWLEDGMENTS

We thank Angstrom Engineering and Innovative Technology for useful discussions regarding material deposition methods and control of glovebox environment, respectively. The authors would like to acknowledge the technical assistance and scientific guidance of E. Palmiano, R. Wolowiec, and D. Kopilovic. This publication is based in part on work supported by Award KUS-11-009-21, made by King Abdullah University of Science and Technology (KAUST), by the Ontario Research Fund Research Excellence Program, and by the Natural Sciences and Engineering Research Council (NSERC) of Canada. D.Z. acknowledges financial support through the NSERC CGS D Scholarship. The manuscript was written through contributions of all authors. All authors have given approval to the final version of the manuscript.

■ REFERENCES

(1) Henry, C. H. *J. Appl. Phys.* **1980**, *51*, 4494−4500.
(2) Sargent, E. H. *Nat. Photonics* **2009**, *3*, 325−331.
(3) Green, M. A.; Emery, K.; Hishikawa, Y.; Warta, W.; Dunlop, E. D. *Prog. Photovolt.* **2012**, *20*, 12−20.
(4) Wang, X.; Koleilat, G. I.; Tang, J.; Liu, H.; Kramer, I. J.; Debnath, R.; Brzozowski, L.; Barkhouse, D. A. R.; Levina, L.; Hoogland, S.; Sargent, E. H. *Nat. Photonics* **2011**, *5*, 480−484.
(5) Ma, W.; Swisher, S. L.; Ewers, T.; Engel, J.; Ferry, V. E.; Atwater, H. A.; Alivisatos, A. P. *ACS Nano* **2011**, *5*, 8140−8147.
(6) Leschkies, K. S.; Beatty, T. J.; Kang, M. S.; Norris, D. J.; Aydil, E. S. *ACS Nano* **2009**, *3*, 3638−3648.
(7) Ma, W.; Luther, J. M.; Zheng, H.; Wu, Y.; Alivisatos, A. P. *Nano Lett.* **2009**, *9*, 1699−1703.
(8) Gao, J.; Perkins, C. L.; Luther, J. M.; Hanna, M. C.; Chen, H.-Y.; Semonin, O. E.; Nozik, A. J.; Ellingson, R. J.; Beard, M. C. *Nano Lett.* **2011**, *11*, 3263−3266.
(9) Gao, J.; Luther, J. M.; Semonin, O. E.; Ellingson, R. J.; Nozik, A. J.; Beard, M. C. *Nano Lett.* **2011**, *11*, 1002−1008.
(10) Brown, P. R.; Lunt, R. R.; Zhao, N.; Osedach, T. P.; Wanger, D. D.; Chang, L.-Y.; Bawendi, M. G.; Bulović, V. *Nano Lett.* **2011**, *11*, 2955−2961.
(11) Liu, H.; Tang, J.; Kramer, I. J.; Debnath, R.; Koleilat, G. I.; Wang, X.; Fisher, A.; Li, R.; Brzozowski, L.; Levina, L.; Sargent, E. H. *Adv. Mater.* **2011**, *23*, 3832−3837.
(12) Wang, X.; Koleilat, G. I.; Fischer, A.; Tang, J.; Debnath, R.; Levina, L.; Sargent, E. H. *ACS Appl. Mater. Interfaces* **2011**, *3*, 3792−3795.
(13) Kramer, I. J.; Sargent, E. H. *ACS Nano* **2011**, *5*, 8506−8514.
(14) Talapin, D. V.; Murray, C. B. *Science* **2005**, *310*, 86−89.
(15) Geyer, S. M.; Allen, P. M.; Chang, L.-Y.; Wong, C. R.; Osedach, T. P.; Zhao, N.; Bulovic, V.; Bawendi, M. G. *ACS Nano* **2010**, *4*, 7373−7378.
(16) Zhitomirsky, D.; Furukawa, M.; Tang, J.; Sadler, P.; Hoogland, S.; Voznyy, O.; Liu, H.; Sargent, E. H. *Adv. Mater*, **2012**, accepted.
(17) Klem, E. J. D.; Shukla, H.; Hinds, S.; MacNeil, D. D.; Levina, L.; Sargent, E. H. *Appl. Phys. Lett.* **2008**, *92*, 212105.
(18) Tang, J.; Kemp, K. W.; Hoogland, S.; Jeong, K. S.; Liu, H.; Levina, L.; Furukawa, M.; Wang, X.; Debnath, R.; Cha, D.; Chou, K. W.; Fischer, A.; Amassian, A.; Asbury, J. B.; Sargent, E. H. *Nat. Mater.* **2011**, *10*, 765−771.
(19) Luther, J. M.; Law, M.; Beard, M. C.; Song, Q.; Reese, M. O.; Ellingson, R. J.; Nozik, A. J. *Nano Lett.* **2008**, *8*, 3488−3492.
(20) Zhao, N.; Osedach, T. P.; Chang, L.-Y.; Geyer, S. M.; Wanger, D.; Binda, M. T.; Arango, A. C.; Bawendi, M. G.; Bulovic, V. *ACS Nano* **2010**, *4*, 3743−3752.
(21) Jasieniak, J.; Califano, M.; Watkins, S. E. *ACS Nano* **2011**, *5*, 5888−5902.
(22) Hyun, B.-R.; Zhong, Y.-W.; Bartnik, A. C.; Sun, L.; Abruña, H. D.; Wise, F. W.; Goodreau, J. D.; Matthews, J. R.; Leslie, T. M.; Borrelli, N. F. *ACS Nano* **2008**, *2*, 2206−2212.

(23) Hines, M. A.; Scholes, G. D. *Adv. Mater.* **2003**, *15*, 1844−1849.
(24) Tang, J.; Brzozowski, L.; Barkhouse, D. A. R.; Wang, X.; Debnath, R.; Wolowiec, R.; Palmiano, E.; Levina, L.; Pattantyus-Abraham, A. G.; Jamakosmanovic, D.; Sargent, E. H. *ACS Nano* **2010**, *4*, 869−878.